Impurities and Electronic Property Variations of Natural MoS_2 Crystal Surfaces

Rafik Addou,*,† Stephen McDonnell,† Diego Barrera,†,‡ Zaibing Guo,§ Angelica Azcatl,† Jian Wang,† Hui Zhu,† Christopher L. Hinkle,† Manuel Quevedo-Lopez,† Husam N. Alshareef,∥ Luigi Colombo,⊥ Julia W. P. Hsu,† and Robert M. Wallace*,†

†Department of Materials Science and Engineering, The University of Texas at Dallas, 800 Campbell Road, Richardson, Texas 75080, Unites States, ‡Centro de Investigación en Materiales Avanzados, S.C. (CIMAV), Unidad Monterrey, Alianza Norte 202, 66600 Apodaca, Nuevo León México, §Core Laboratories, and ∥Materials Science and Engineering King Abdullah University of Science and Technology (KAUST), Thuwal 23955-6900, Saudi Arabia, and ⊥Texas Instruments Incorporated, 13121 TI Boulevard, MS-365, Dallas, Texas 75243, Unites States

ABSTRACT Room temperature X-ray photoelectron spectroscopy (XPS), inductively coupled plasma mass spectrometry (ICPMS), high resolution Rutherford backscattering spectrometry (HR-RBS), Kelvin probe method, and scanning tunneling microscopy (STM) are employed to study the properties of a freshly exfoliated surface of geological MoS_2 crystals. Our findings reveal that the semiconductor 2H-MoS_2 exhibits both n- and p-type behavior, and the work function as measured by the Kelvin probe is found to vary from 4.4 to 5.3 eV. The presence of impurities in parts-per-million (ppm) and a surface defect density of up to 8% of the total area could explain the variation of the Fermi level position. High resolution RBS data also show a large variation in the MoS_x composition ($1.8 < x < 2.05$) at the surface. Thus, the variation in the conductivity, the work function, and stoichiometry across small areas of MoS_2 will have to be controlled during crystal growth in order to provide high quality uniform materials for future device fabrication.

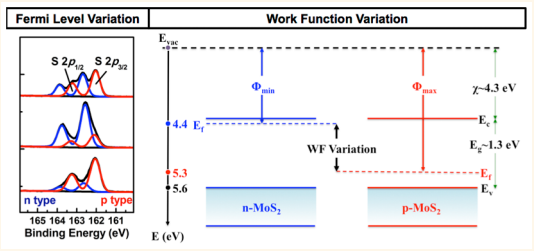

KEYWORDS: MoS_2 · Fermi level shift · surface defects · X-ray photoelectron spectroscopy · impurities · work function · scanning tunneling microscopy · electron affinity

Molybdenite, MoS_2, is the most investigated transition metal dichalcogenide because of its abundance in nature,[1] sizable specimens (~ cm^2), commercial availability, and promising properties. In addition to its widespread use for tribological applications,[2] MoS_2 is being evaluated for and is being integrated into different devices in nanoelectronics,[3,4] optoelectronics,[5,6] biosensors,[7] hydrogen production,[8,9] and water purification[10] among others. The aforementioned devices typically contain heterostructures with the associated interfaces between the various materials, including potential contaminant residues introduced during the fabrication process. These interfaces play a critical role in device performance[11] and need to be carefully controlled. In this regard, although typically ignored in many studies, it is critical to consider the role of native defects, impurities, and reaction of the MoS_2 with the ambient before any device fabrication process.

Despite the promising electronic applications of MoS_2, several erratic behaviors have been observed in devices fabricated using exfoliated geological MoS_2. For example, I–V characteristics measured on bare MoS_2 or after metal deposition show large variability across the surface.[12] A low electron Schottky barrier height (SBH) and Ohmic contacts have been reported with metals that have a large work function, for example, W, Au, Pd, and Ni, and that would be expected to form a high electron Schottky barrier with MoS_2.[12−20] In another study,[21] the conductivity polarity measured on gold nanoparticles deposited on MoS_2 using I–V and Raman measurements also showed substantial inconsistencies. In that study, the n- and p-type behavior was measured on samples that were prepared in an identical manner and the variability was explained

* Address correspondence to addou@utdallas.edu, rmwallace@utdallas.edu.

Received for review June 2, 2015 and accepted August 22, 2015.

Published online August 24, 2015
10.1021/acsnano.5b03309

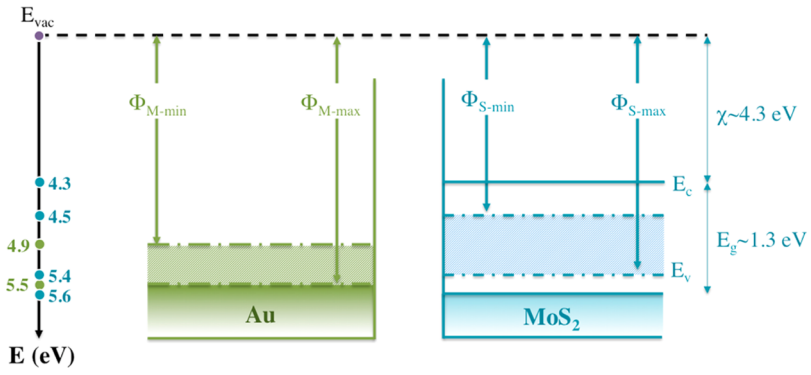

Figure 1. Simplified schematic of the energy band lineup at the interface between Au metal and MoS_2 crystal. $\Phi_{M\text{-}min}$ and $\Phi_{M\text{-}max}$ represent the lowest and the highest Au work function reported in literature, respectively. Similarly, $\Phi_{S\text{-}min}$ and $\Phi_{S\text{-}max}$ indicate the work function range reported for MoS_2.

by the difference in MoS_2 thickness and/or by the Au-MoS_2 interface interaction.[21] Furthermore, while MoO_x deposited on MoS_2 under UHV conditions resulted in core-level band bending that suggested an Ohmic contact, devices fabricated using MoO_x in a high vacuum ($\sim 10^{-6}$ *Torr*) but not UHV showed a low Schottky barrier for holes. The discrepancy between the two approaches was explained by a lower work function of MoO_x deposited in high vacuum in comparison with MoO_x deposited in UHV.[22,23]

The reported conductivity type induced by metals deposited on MoS_2 depends strongly on the work function of both the metal and the MoS_2 substrate. Several studies indicate that the MoS_2 work function (Φ_S) varies between 4.5 and 5.4 eV,[24−28] the electron affinity (χ) is reported to be ~4.3 eV,[23,32] and the work function reported for Au (Φ_M) ranges between 4.9 and 5.5 eV.[29−31] Figure 1 illustrates the proposed energy band alignment at the Au/MoS_2 interface with the work function variability reported above. The band diagram displays both upward and downward band bending when the Au interfaces with MoS_2. For example, downward band bending occurs at an interface where $\Phi_M < \Phi_S$ while upward band bending occurs when $\Phi_M > \Phi_S$. Characterization of various metal contacts on MoS_2 performed by two different research groups reveals the presence of pinning behavior,[12,19] which deviates from the Schottky-Mott equation ($\Phi_B = \Phi_M - \chi$).[17,19] Both n- and p-type behavior were observed on the bare surface and after metal deposition.[12] The current densities show the same trend with vacuum work function of the metal.[12,19] In general, while the large variability can easily be explained by chemical interactions occurring at the interface in certain cases, a combination of Fermi level pinning and the presence of a high defect density on MoS_2 (up to 8 at. %) explains the variability observed even when no detectable interfacial reactions are observed.

Several studies have shown that bulk MoS_2 is intrinsically an n-type semiconductor with an indirect bandgap of 1.2−1.3 eV for multilayers[32−35] and direct bandgap of 1.8−1.9 eV for monolayer flakes.[34−36] However, p-type behavior was also reported on bulk crystals.[12,23,24,37] The 2H-MoS_2 phase is the most stable among the three established polytypes of MoS_2 (1T, 2H, and 3R)[38] and it is also well-known that the intercalation of alkali metals such as Li, Na, or K into 2H-MoS_2 causes a phase transformation to the distorted 1T′-MoS_2 which exhibits a metallic nature.[39−45]

Surface analysis techniques such as X-ray photoelectron spectroscopy (XPS) have been employed to study such a phase transition from Li intercalation.[42,43] In XPS, all photoelectron energies are referenced to the Fermi level position and the binding energy of the detected peak is a measure of the energy difference between the initial and final states of the atom that has been photoionized.[46] Therefore, it would not be surprising for 2H-MoS_2 and 1T-MoS_2 to exhibit unique spectral features. Moreover, the coexistence of both phases 2H- and 1T-MoS_2 within the same 500 μm^2 analysis area would then be expected to yield two distinct spectra. Such spectral features have also been recently reported after MoS_2 immersion in butyllithium solution[43] and previously after *in situ* UHV dosing of the MoS_2 surface with Li.[42] Recently, the metallic phase of 1T′-MoS_2 produced by lithiation was successfully used to reduce contact resistance.[45] Both photoelectron emission and Raman spectroscopy were used to differentiate between 1T′- and 2H-MoS_2 structures. For the Mo 3d and S 2p core levels from such lithiated samples, the component located at lower binding energy was assigned to the metallic phase 1T′ and the component at higher binding energy to the semiconductor phase 2H.[45]

In this study, we use several surface and bulk methods to investigate the origin of the variation in MoS_2 properties, which has not been systematically addressed yet in the literature. Photoemission studies reveal the presence of both conductivity types that will be confirmed by band alignments constructed from our work function measurements. STM studies reveal a highly defective surface, which provides dangling

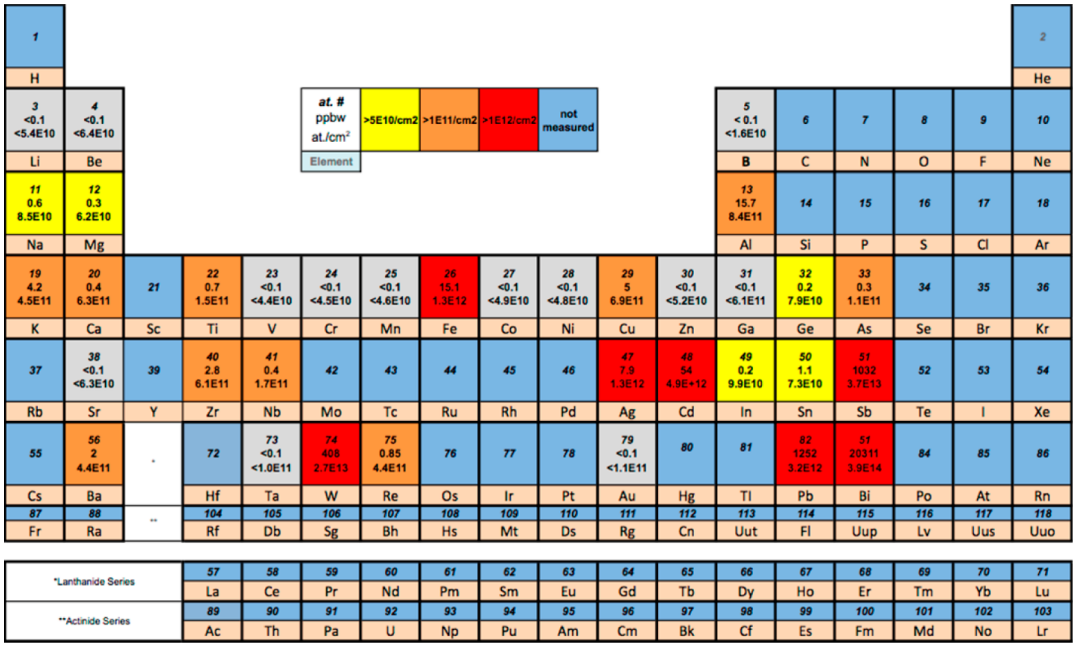

Figure 2. Periodic table shows the impurity concentrations from ICPMS analysis of geological MoS_2. The abundance unit is parts-per-billion by weight (ppbw).

bonds and thus reaction upon atmospheric exposure. The variability and reactivity of the MoS_2 surface are also shown to be significant and must be mitigated to enable high-quality electronic materials for reproducible device fabrication.

RESULTS AND DISCUSSION

Impurity Detection. Several theoretical and experimental studies show that majority charge carriers in geological molybdenite ("g-MoS_2") can be introduced by incorporating foreign atoms, that is, substitutional doping or intercalation.[47,48] Inductively coupled plasma mass spectrometry (ICPMS), with an impurity detection limit better than 1 part-per-billion (ppb) for most impurities, was used to determine the impurity concentration for 33 different elements from acid-digested geological MoS_2 crystal surfaces.[49,50] The ICPMS data reveals a large number of impurities at considerable concentrations. Figure 2 shows all of the impurities detected with concentrations > 0.2 ppb by weight (ppbw). Al, As, Bi, Ca, Cd, Fe, Pb, and W elements are present in concentrations higher than 10 ppbw, and many of these are known to have energy levels within the bandgap of silicon.[51] Also, it is likely that many of them will be electrically active in MoS_2 in various allowed sites and in general other transition metal dichalcogenide (TMD) materials as well. An estimate of the equivalent impurity concentration levels shows that this can easily exceed $5 \times 10^{10}/cm^2$ (Figure 2), and thus the presence of ionized impurities is expected to have a high impact in carrier transport measurements.[52,53] High resolution XPS was also used to search for foreign elements; however, except for C and O all other impurities were found to be below XPS detection limits (Figure S1); this is expected since XPS has a detection limit on the order of 0.05%, which is significantly higher than ICPMS, but is illustrative in that the detection of impurities, potentially responsible for degrading materials properties such as mobility, must be carefully considered and is not typically discussed in the recent device literature. We also examined MoS_2 samples by time-of-flight secondary ion mass spectrometry (ToF-SIMS) which has a detection limit higher than ICPMS and identified the following impurities: Al, Fe, Si, Cu, Mn, Cr, Ni, B, and V (Supporting Information, Table S3).

Importantly, the comparison of the ICPMS results between a synthetic MoS_2 (s-MoS_2) by chemical vapor transport and g-MoS_2 sample (Table S1 and S2) at this early stage of development reveals the presence of high level of impurities, *regardless of the source*. This result highlights the need for continued improved synthesis process to ensure that higher purity materials are made available for integration into nanoelectronic devices. Moreover, the concentration level in some impurities such as Ag, As, Ba, Bi, Fe, Mg, and W is higher in the synthetic sample s-MoS_2 than in g-MoS_2. Further comparative study of this vapor-deposited MoS_2 is of great interest and is underway.

n- and p-type Conductivity in MoS_2: Photoemission Study. X-ray photoelectron spectroscopy was used to study the chemical state of exfoliated MoS_2(0001) surface. Only two contaminant species are detected by XPS: carbon and oxygen (occasionally and in low concentrations) consistent with the previous reports (Figure S1).[12,33] In separate experiments it was shown that annealing in

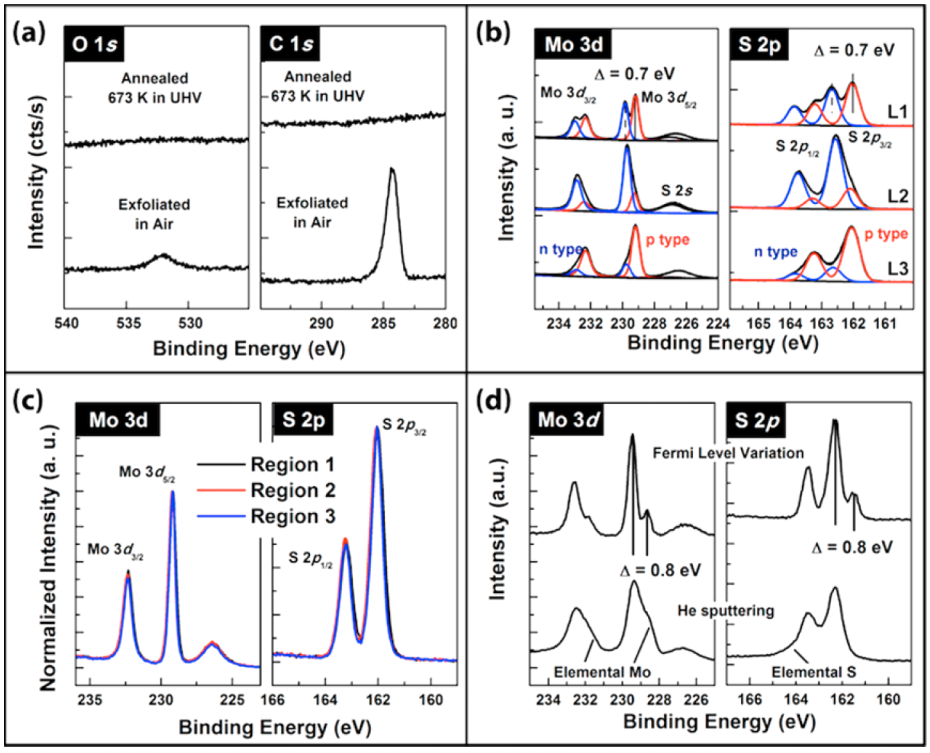

Figure 3. (a) O 1s and C 1s core levels peaks prior and after annealing g-MoS_2 in UHV to 400 °C for 15 min. (b) Mo 3d and S 2p core levels measured on three different locations. L1 and L2 are acquired on the same sample. For clarity, the n- and p-type components in spectra L3 are aligned with L2. (c) On the third sample, three different locations showing no Fermi level variation. (d) Comparison between the Fermi level variation on as-exfoliated MoS_2 crystal and He sputtered MoS_2 surface.

UHV up to 400 °C for 15 *min* is sufficient to render the surface contaminants below the limit of detection by XPS (Figure 3a). Nevertheless, the XPS measurements reveal considerable spatial variability across the surface of a single sample. The spot size used during the XPS acquisition is approximately 0.5 mm in diameter. The spatial variability is observed by scanning a different location separated by less than 1 mm. Figure 3b shows a comparison between the surface characteristics observed across a single sample (L1 and L2) and the spectra obtained from a different sample (L3). On one region (L2), the expected peaks of Mo $3d_{5/2}$ (S $2p_{3/2}$) corresponding to n-type MoS_2 are measured at 229.7 eV (162.55 eV), in agreement with the reported binding energies.[12,54] Concurrently, a second feature at lower binding energy is also identified confirming the presence of the second component that may be responsible for the p-type behavior, with core levels shifted to 229.2 eV (162.05 eV) for Mo $3d_{5/2}$ (S $2p_{3/2}$). On another area (L1), XPS measurements indicate the presence of both features, expressed by two pronounced single peaks Mo $3d_{5/2}$ (S $2p_{3/2}$) located at 229.0 eV (161.9 eV) for p-type peak and at 229.7 eV (162.55 eV) for n-type peak. On another MoS_2 sample, the spectra L3 in Figure 3b show the presence of a shoulder at higher binding energy for both Mo 3d and S 2p core levels. The main peak for Mo $3d_{5/2}$ and S $2p_{3/2}$ is assigned to p-type MoS_2 while the higher binding energy shoulder (blue peak, L3) is assigned to n-type MoS_2. The n-type component is less pronounced in this region of the sample. The stoichiometry of MoS_x estimated from all of the analyzed spectra indicates the presence of large variations in the S concentrations, leading to an alloy ratio x in MoS_x ranging from 1.6 to 2.1.

Similarly, the XPS performed on another g-MoS_2 sample also showed oxygen and carbon only as expected. The spectra shown in Figure 3c are acquired from a single sample, but are not typical of MoS_2 evaluated so far, as they displayed no variability between the areas of the sample that were analyzed. While low levels of variability were occasionally observed, the spectra displayed in Figure 3b are more representative of the typical characteristics of MoS_2. The core-levels acquired at three different locations on the same sample (Figure 3c) show perfect alignment with core levels position consistent with p-type behavior; this sample exhibits a higher degree of uniformity than is typically observed.

The large spatial variability in the electronic properties of MoS_2 observed on different samples (Figure 3b,c) reveals the difficulty in correctly identifying (or assigning) unique conductivity behavior. As discussed in the introduction, similar low binding energy components in the Mo 3d and S 2p have previously been correlated with the formation of metallic distorted 1T′-MoS_2 after alkali exposure.[42,43,45] It should therefore be noted that in this present study, the MoS_2 was mechanically exfoliated in air with *no intentional exposure to alkali metals*,

and none were detected by XPS as natural contaminants (Supporting Information, Figure S1). The high concentration of some alkali elements detected by ICPMS and SIMS does not result in phase transformations as the STS measurements always show a detectable band gap. It is also important again to highlight that either conductivity variations or the 2H to distorted 1T phase transformation can result in very similar core-level spectra; thus, the XPS spectra alone are not sufficient to provide direct, unique evidence of either phenomenon. Instead, it should be interpreted as evidence of local variations in Fermi-level that may originate from very different mechanisms. Other characterization techniques such as Raman spectroscopy, X-ray diffraction, and current−voltage measurement can help to distinguish between these two causes.

To demonstrate that the second feature detected in the XPS spectra is not caused by a chemical bonding shift, an MoS_2 surface was intentionally sputtered by a He^+ ion beam at 1 keV. This process creates a different chemical environment through ion-beam mixing and defect production, that is, MoS_2 and MoS_x. Figure 3d compares the Fermi level variation measured on a pristine surface and the chemical change induced by sputtering. On the as-exfoliated surface, shoulders in both the Mo 3d and S 2p are shifted to lower binding energy by the same peak separation (Δ = 0.8 eV). On the sputtered surface, a low binding energy feature is still present in the Mo 3d core-level, however no similar shift was detected at lower binding energy for S 2p core-level. Therefore, the low binding energy feature in this case for the Mo 3d after He sputtering cannot be explained by Fermi level variations, since Fermi level variations will alter the binding energy position of all elemental core-levels detected equally. Instead, this feature from the sputtered sample suggests the presence of metallic Mo caused by sulfur loss from the top surface region. There is additional evidence of a chemical change found in the S 2p core-level. A high binding energy shoulder is observed after sputtering suggesting the presence of elemental sulfur. This result highlights the importance of using both the Mo 3d and the S 2p core-level when attempting to distinguish between chemical changers and variations in Fermi level. A similar behavior was observed previously by noble gas ion bombardment on the basal plane surface of crystalline and polycrystalline MoS_2.[55,56] The sputtering results in substantial sulfur reduction or a Mo rich film, and a number of different molybdenum−sulfur (MoS_x) and molybdenum−oxide (MoO_x) species.

Variation in the MoS_x Stoichiometry. High-resolution Rutherford backscattering spectrometry, HR-RBS, is one of the most effective methods for near-surface layer analysis of materials, chemical composition, and depth profiling of individual elements. The main goal of using RBS is to study the variation of the MoS_x stoichiometry near the surface. Figure 4 shows the

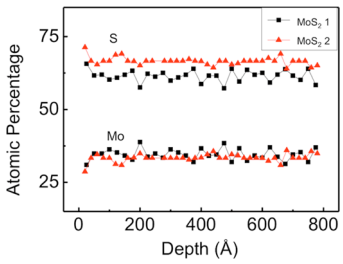

Figure 4. Comparison of the elemental composition of two different MoS_2 using high resolution Rutherford backscattering spectrometry. The MoS_2-1 sample is more S-deficiency than MoS_2-2.

TABLE 1. Workfunction (Φ) and Valence Band Maximum (VBM, IE) Measurements on Two Different Samples before and after 25 min from Exfoliation

MoS_2 crystal	g-MoS_2-A		g-MoS_2-B	
exfoliation	before	after	before	after
Φ (eV)	5.19 ± 0.01	5.16 ± 0.01	4.87 ± 0.01	4.85 ± 0.01
IE (eV)	5.68 ± 0.05	5.64 ± 0.05	5.66 ± 0.05	5.61 ± 0.05

HR-RBS depth profile measured on two different samples (MoS_2-1 and MoS_2-2) indicating that the atomic concentration varies significantly throughout the investigated depth (80 nm). The data show that the S concentration of one sample is lower, Mo-rich, in comparison to that of the other MoS_2 sample. The average composition across the 80 nm depth-profile shows that the MoS_2-2 is sulfur deficient with (S/Mo) = x = 1.8 (*i.e.*, $MoS_{1.8}$), while that the MoS_2-1 sample is slightly Mo-rich with x = 2.05 (*i.e.*, $MoS_{2.05}$). The variation in the MoS_x stoichiometry on or at the vicinity of the surface may contribute to the variation in the conductivity-type as detected by different measurement techniques such as XPS, as well as the correlation to structural defects recorded by STM/STS.[12,33]

Work Function Variation and Ionization Energy. The work function (Φ) variation of two different MoS_2 samples was measured in air by the Kelvin probe technique before and after exfoliation (Table 1). Such surfaces are anticipated to be representative of those produced by exfoliation typically used for device fabrication. Prior to exfoliation, the Φ value is measured to be Φ (g-MoS_2-A)$_{before}$ = 5.19 ± 0.01 eV and Φ (g-MoS_2-B)$_{before}$ = 4.87 ± 0.01 eV. The Φ measured within 1 min of the exfoliation process decreases with time and then stabilizes after about 25 min (Figure 5a) in a laboratory ambient. The time dependent behavior could arise from the adsorption of contaminants from the atmosphere (*e.g.*, hydrocarbons, water, *etc.*) or oxidation. The work function values stabilize close to the pre-exfoliated surface value after 30 min exposure to the ambient with the following values: Φ (g-MoS_2-A)$_{after}$ = 5.16 ± 0.01 eV and Φ (g-MoS_2-B)$_{after}$ = 4.85 ± 0.01 eV. It should be noted that such differences in the

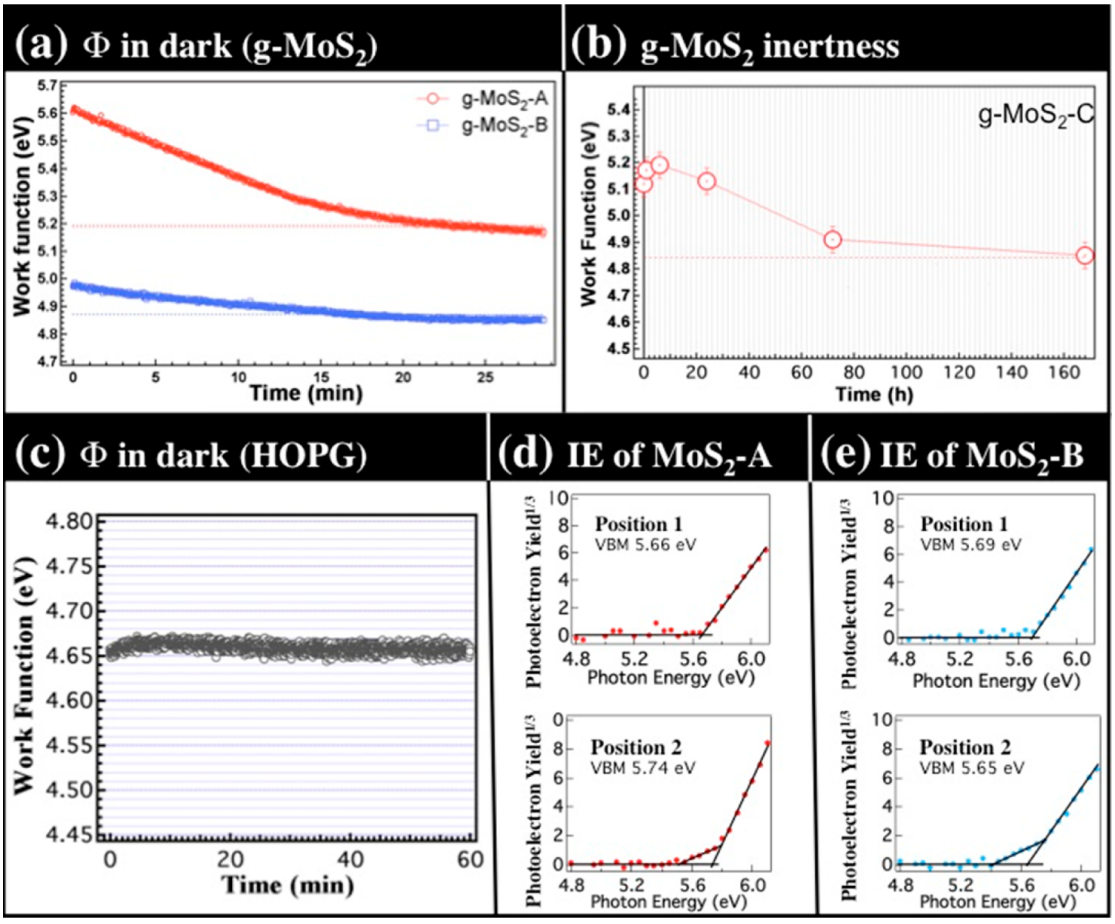

Figure 5. (a) Kelvin probe measurement of the Φ of two different samples g-MoS_2-A and g-MoS_2-B; (b) Φ evolution recorded on another (g-MoS_2-C) freshly exfoliated surface (0 h) until reaching the initial value (dashed line) after a week (168 h) in air; (c) Φ measurements on as-exfoliated HOPG. The HOPG Φ averaged from 3000 measurements during 1 *h* is 4.66 eV. Panels d and e show the ionization energy measurement of g-MoS_2-A and g-MoS_2-B, respectively. The position 2 shows a second slope likely caused by the presence of traps on the surface.[59] The photoemission threshold energy for this second slope is 5.40 eV.

experimental work function are consistent with the stoichiometry variation in the sulfur concentrations in MoS_2, as measured by RBS and XPS. The surface characteristics of the synthesized MoS_2 studied using STM and Kelvin probe measurements show comparable results indicative of a defective surface. (Figure S4 and S5).

Different samples examined under identical ambient conditions show significant variations in the Φ. The highest Φ value obtained on the air-exposed, as-exfoliated sample (>25 min) was measured at 5.33 eV and the lowest value at 4.45 eV (Supporting Information, Table S4 and S5). On yet another sample g-MoS_2-C (see Figure 5b), the Φ after exfoliation reaches the value prior to exfoliation in a period of 7 days as shown in Figure 5b, which indicates that it takes much longer for the surface of this sample to be saturated with ambient contaminants; this sample also showed non-monotonic time dependence during the first 6 h after exfoliation. To compare this time dependent variation on another van der Waals material, the Φ of highly ordered pyrolytic graphite (HOPG) was measured under the same ambient conditions for the first hour after exfoliation. Figure 5c shows that the Φ of HOPG is stable in air with a variation of only between 4.64 and 4.67 eV indicative of the chemical stability of the sp^2 surface and in good agreement with literature.[57] The reactivity of the MoS_2 surface with oxygen, and the impact on the electronic structure, has been recently studied using density functional theory.[58] Calculations indicate that the air stability of MoS_2 and the electronic band gap are significantly impacted by the presence of surface defects and increasing O concentration.[58]

The ionization energy (IE) was measured using photoelectron spectroscopy in air (PESA). Figure 5d,e shows the PESA results for each sample at two different positions. Each IE value in Table 1 was obtained as an average from 7 measurements. The threshold of $(\text{photoelectron yield})^{1/3}$ as a function of the UV excitation energy is the IE, that is, valence band maximum (VBM) position, of the sample. The IE values measured before and after exfoliation are almost identical and within the uncertainty of the instrument. Also, the IE is similar for both MoS_2 samples corresponding to the value of 5.65 ± 0.05 eV which is similar to that reported by Schlaf *et al.*[27] The only variability observed in the IE measurements across a single crystal surface is the

occasional presence of a second slope (position 2, Figure 5d,e). The presence of a second slope is in agreement with the spatial variation measured by photoemission and can also be explained by the presence of a surface layer with lower IE values (~5.40 eV).[59] Taking a bandgap of 1.3 eV measured by scanning tunneling spectroscopy,[33] the measured Φ indicates the presence of both polarities as sketched in Figure 6. The estimated electron affinity of about 4.35 ± 0.05 eV is in agreement with recently corrected electron affinity.[23]

Surface Defects. Room temperature STM was employed to study the surface characteristics of natural MoS_2 along the basal plane.[33] Figure 7a,b shows STM images recorded at different locations on the same freshly exfoliated surface, the defect density of the dark defects varies across a single sample. The characteristics of the defects also change in depth (0.6−1.8 nm), width (3−5 nm), and nature (structural, metallic-like, impurities, and point defects).[33] A single defect is presented in Figure 7c with ~3 nm in width and ~0.6 nm in depth as dimensions. Such defects are likely responsible for the presence of dangling bonds,[60] and thus the reactivity of the 2D material will be strongly increased, relative to an ideal, pristine surface. The variation in the measured work function in air observed from sample to sample will change depending on the concentration of imperfections and stoichiometry, and some of these intrinsic defects on van der Waals surfaces can be very active and may act as nucleation centers.[61] The presence of these surface defects and their role in surface reactions can be correlated to the decay in the work function measurement during the first 30 min after exfoliation and the different behavior in air measured by Kelvin probe. We also used STM and STS to characterize the surface of synthetic MoS_2. The results presented in Figure S3 (Supporting Information) reveal that the surface characteristics and the quality of s-MoS_2 are not different than the g-MoS_2, suggesting that the spatial variation observed in both s-MoS_2 and g-MoS_2 can be explained by the presence of impurities and imperfections.

In summary, the exfoliated molybdenite surface typically used for device fabrication as reported in the recent literature shows large spatial variations of the Fermi level position. By considering that the XPS core levels are measured with respect to the Fermi level, the local variation is explained by the presence of both conductivity polarities (n and p). The Mo 3d core-levels observed in this study, show that the ratio of the two components also varies with position across the investigated MoS_2(0001) surface. Only two impurities (C and O) are detected within the limits of detection by XPS. However, significant concentrations of impurities such as Al, B, Cr, Cu, Fe, Mn, Mg, Na, Nb, Ni, Re, V, and W were detected in parts per billion and in parts per million by ICPMS. Such concentrations are expected to readily cause n- and p-type conductivity behavior,[47] and also impact transport properties and variability.[52,53] Both XPS and HR-RBS show that the molybdenite chemical composition in the near surface region is not uniform, with substantial variations in sulfur concentration, and results in a spatially variable chemical reactivity after exfoliation. This chemical variation might explain the lower IE slope in PESA measurements and a large change in the work function. On the basis of a bandgap of ~1.3 eV, the midgap energy is equal to 4.95 eV. The work function measured by the Kelvin probe shows values ranging from 4.4 to 5.3 eV, illustrating the existence of both n- and p-conduction (as illustrated in Figure 6). Further, STM analysis reveals large variation at the nanometer scale and across the

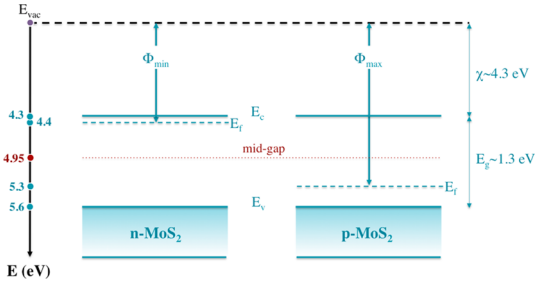

Figure 6. Band diagram constructed from the work function measurements on two different MoS_2 crystals, and using the measured values of electron affinity (χ = 4.3 eV) and bandgap (E_g = 1.3 eV).

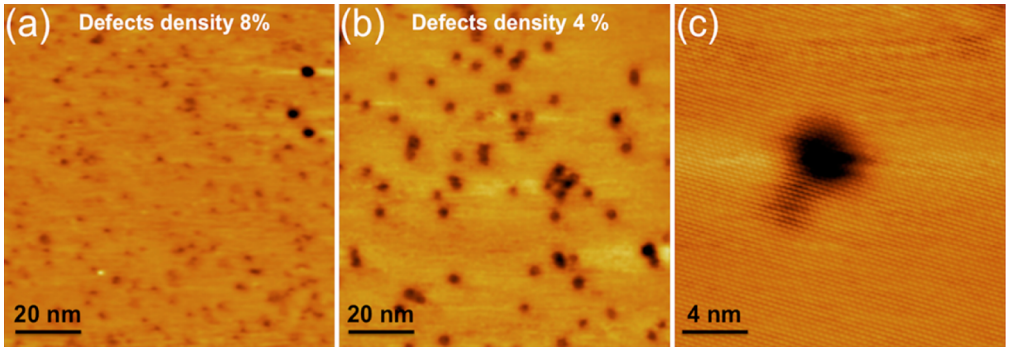

Figure 7. Defect density changes across the same MoS_2 surface. (a) STM image (V_{bias} = 1.15 V, I_t = 0.5 nA) and (b) (V_{bias} = 0.75 V, I_t = 1 nA) recorded on different locations. (c) STM image (V_{bias} = −0.15 V, I_t = 3 nA) shows a high magnification on a dark defect.

whole crystal surface. Finally, the surface structure exhibits several type of imperfections: S-vacancies, donor and acceptor impurities, and structural defects with different width and depth and the resulting local electronic structure confirms the variability in the Fermi level position.[12,33]

CONCLUSIONS

The results presented in this paper point out that the measured n- and p-type conductivity characteristics of exfoliated, geological molybdenite are not necessarily caused by any intentional thermal or chemical treatment after growth. Rather, imperfections and impurities can generate spatial variations in the conductivity. Freshly exfoliated MoS_2 from different sources displays large variability over areas smaller than 500 μm^2 on the same MoS_2 crystal surface. The variability can be associated with nonstoichiometry as well as the detection of structural defects and impurities, as revealed by STM, XPS, RBS, ToF-SIMS, and ICPMS. The presence of such imperfections in geological MoS_2 induces discrepancies in the work function as measured by Kelvin probe. Therefore, it is indispensable to understand and to account for the fact that such variations are likely present in current device fabrication processes incorporating g-MoS_2, even without further extrinsic contaminants/residues, such as that from polymers utilized in lithography steps. Moreover, it is also seen that synthetic MoS_2 bulk crystals can exhibit similar properties.

Finally, these results are consistent with prior studies indicating that the structural defects on exfoliated MoS_2 result in the formation of dangling bonds, causing a more reactive MoS_2 surface in air that can lead to bonding with air contaminants such as oxygen, H_2O, and hydrocarbons.[12,33,58,60] Our findings indicate that the variation at the micrometer scale can be interpreted and related to the nanoscale variation. For reliable, reproducible, and manufacturable 2D devices, homogeneous and high quality MoS_2 (and other TMDs) is urgently needed, and any future work will have to be focused on reducing the density of such imperfections (e.g., vacancies, grain boundaries, various structural defects, and impurities). Enormous efforts are now underway on the growth of high quality (i.e., structural and low-impurity) TMD materials using a variety methods, and the understanding and control of defect physics and chemistry in these materials is of utmost importance in order to achieve high quality devices.[62−65]

MATERIALS AND METHODS

The preparation of the MoS_2 crystal surface consists of mechanical cleaving (exfoliation) in air using scotch tape.[66] After exfoliation, the bulk crystal (lateral size > 5 mm, thickness > 0.1 mm)[67] is loaded within 1 min to a UHV system with a base pressure better than 2×10^{-10} mbar using a fast entry lock ($P_{FEL} \approx 10^{-7}$ mbar). The UHV system is a customized Omicron instrument.[68] The analysis chamber incorporates a monochromated Al Kα X-ray source and a high intensity helium ultraviolet source. The generated photoelectrons are detected by a multichannel plate MCD 128 on an Argus electron analyzer. The spot size used during the acquisition is about 0.5 mm in diameter. Core-level spectra are analyzed with the spectral analysis software AAnalyzer. A coupled chamber houses a variable temperature scanning probe microscope (SPM); the variable temperature design allows analysis using traditional STM methods.[33] The STM images in this study were acquired at room temperature with an etched tungsten tip.

The vapor phase decomposition ICPMS measurements are performed by the Balazs Nanoanalysis lab which provides contamination measurements on Si wafers for the semiconductor industry and is established as the standard for such surface contamination analysis for detection levels well below methods such as XPS. The lab has developed protocols to measure the impurity concentration in the solutions they use for the "etching" of the MoS_2 and then they measure the "digested" surface impurity species on MoS_2, through the formation of fluoride ions from the resultant vapor.[50] The impurities in the etching solutions are at extremely low levels, nearly undetectable by such mass spectrometry. Impurity measurements are thus confined to the accessible surface region of the MoS_2, as the MoS_2 is relatively inert to chemical attack.

The *ex situ* work function and ionization energy of the samples are measured in air using a Kelvin probe apparatus (SKP 5050, KP Technology) and photoelectron spectroscopy in air (model AC-2, RKI Instruments), respectively. In the Kelvin probe measurements, a stainless steel probe (1 mm diameter, ~4.4 eV work function) is calibrated against a piece of 100 nm thick Au sample (work function equal to 5.15 eV).[29] The instrument resolution is about 3 meV. The ionization energy is determined from the threshold of photoelectron yield to the 1/3 power vs energy taken with 100 nW deuterium lamp intensity and energy scanning between 4.8 and 6.2 eV with a step of 0.05 eV and spot size of ~1 mm^2.[69] The HR-RBS analyses were performed in an instrument manufactured by *Kobe Steel, Ltd.* The RBS composition vs depth profile was obtained with 400 keV He^+ ions with a beam size about 1 mm^2.[70]

Conflict of Interest: The authors declare no competing financial interest.

Acknowledgment. The authors thank Dr. Monte Douglas (Texas Instruments) for the ToF-SIMS analysis and Ms. Zeyan Xu. This work was supported in part by the Southwest Academy on Nanoelectronics (SWAN) sponsored by the Nanoelectronic Research Initiative and also by the Center for Low Energy Systems Technology (LEAST), one of six centers supported by the STARnet phase of the Focus Center Research Program (FCRP), a Semiconductor Research Corporation program sponsored by MARCO and DARPA, and the US/Ireland R&D Partnership (UNITE) under the NSF award ECCS-1407765. D.B. acknowledges the support of Consejo Nacional de Ciencia y Tecnología (CONACyT) and Project NL-2010-C33-149216. J.W.P.H. acknowledges the support from Texas Instruments Distinguished Chair in Nanoelectronics.

Supporting Information Available: The Supporting Information is available free of charge on the ACS Publications website at DOI: 10.1021/acsnano.5b03309.

Comparison of impurity elements detected by ICPMS between synthetic and geological MoS_2, ToF-SIMS intensities, XPS measurements of impurities, additional work function measurements on different crystals and across the same surface, and surface characterization of the synthetic MoS_2 using STM/STS, Kelvin probe, and PESA (PDF)

REFERENCES AND NOTES

1. Golden, J.; McMillan, M.; Downs, R. T.; Hystad, G.; Goldstein, I.; Stein, H. J.; Zimmerman, A.; Sverjensky, D. A.; Armstrong, J. T.; Hazen, R. M. Rhenium Variations in Molybdenite (MoS_2): Evidence for Progressive Subsurface Oxidation. *Earth Planet. Sci. Lett.* **2013**, *366*, 1–5.
2. Winer, W. O. Molybdenum Disulfide as a Lubricant: A Review of the Fundamental Knowledge. *Wear* **1967**, *10*, 422–452.
3. Wang, Q. H.; Kalantar-Zadeh, K.; Kis, A.; Coleman, J. N.; Strano, M. S. Electronics and Optoelectronics of Two-Dimensional Transition Metal Dichalcogenides. *Nat. Nanotechnol.* **2012**, *7*, 699.
4. Chang, H.-Y.; Yang, S.; Lee, J.; Tao, L.; Hwang, W.-S.; Jena, D.; Lu, N.; Akinwande, D. High-Performance, Highly Bendable MoS_2 Transistors with High-K Dielectrics for Flexible Low-Power Systems. *ACS Nano* **2013**, *7*, 5446–5452.
5. Bernardi, M.; Palummo, M.; Grossman, J. C. Extraordinary Sunlight Absorption and One Nanometer Thick Photovoltaics Using Two-dimensional Monolayer Materials. *Nano Lett.* **2013**, *13*, 3664–3670.
6. Tsai, M.-L.; Su, S.-H.; Chang, J.-K.; Tsai, D.-S.; Chen, C.-H.; Wu, C.-I.; Li, L.-J.; Chen, L.-J.; He, J.-H. Monolayer MoS_2 Heterojunction Solar Cells. *ACS Nano* **2014**, *8*, 8317–8322.
7. Sarkar, D.; Liu, W.; Xie, X.; Anselmo, A. C.; Mitragotri, S.; Banerjee, K. MoS_2 Field-Effect Transistor for Next-Generation Label-Free Biosensors. *ACS Nano* **2014**, *8*, 3992–4003.
8. Xiang, Q.; Yu, J.; Jaroniec, M. Synergetic Effect of MoS_2 and Graphene as Cocatalysts for Enhanced Photocatalytic H_2 Production Activity of TiO_2 Nanoparticles. *J. Am. Chem. Soc.* **2012**, *134*, 6575–6578.
9. Ataca, C.; Ciraci, S. Dissociation of H_2O at the Vacancies of Single-Layer MoS_2. *Phys. Rev. B: Condens. Matter Mater. Phys.* **2012**, *85*, 195410.
10. Tacchini, I.; Terrado, E.; Anson, A.; Martinez, M. T. Preparation of a TiO_2-MoS_2 Nanoparticle-Based Composite by Solvothermal Method with Enhanced Photoactivity for the Degradation of Organic Molecules in Water Under UV Light. *Micro Nano Lett.* **2011**, *6*, 932–936.
11. Coy-Diaz, H.; Avila, J.; Chen, C.; Addou, R.; Asensio, M. C.; Batzill, M. Direct Observation of Interlayer Hybridization and Dirac Relativistic Carriers in Graphene/MoS_2 van der Waals Heterostructures. *Nano Lett.* **2015**, *15*, 1135–1140.
12. McDonnell, S.; Addou, R.; Buie, C.; Wallace, R. M.; Hinkle, C. L. Defect-Dominated Doping and Contact Resistance in MoS_2. *ACS Nano* **2014**, *8*, 2880–2888.
13. Gourmelon, E.; Bernede, J. C.; Pouzet, J.; Marsillac, S. Textured MoS_2 Thin Films Obtained on Tungsten: Electrical Properties of the W/MoS_2 Contact. *J. Appl. Phys.* **2000**, *87*, 1182–1186.
14. Radisavljevic, B.; Radenovic, A.; Brivio, J.; Giacometti, V.; Kis, A. Single-Layer MoS_2 Transistors. *Nat. Nanotechnol.* **2011**, *6*, 147.
15. Liu, H.; Neal, A. T.; Ye, P. D. Channel Length Scaling of MoS_2 MOSFETs. *ACS Nano* **2012**, *6*, 8563–8569.
16. Liu, H.; Neal, A. T.; Du, Y.; Ye, P. D. Fundamentals in MoS_2 Transistors: Dielectric, Scaling and Metal Contacts. *ECS Trans.* **2013**, *58*, 203–208.
17. Das, S.; Chen, H. Y.; Penumatcha, A. V.; Appenzeller, J. High Performance Multi-Layer MoS_2 Transistors with Scandium Contacts. *Nano Lett.* **2013**, *13*, 100–105.
18. Liu, D.; Guo, Y.; Fang, L.; Robertson, J. Sulfur Vacancies in Monolayer MoS_2 and its Electrical Contacts. *Appl. Phys. Lett.* **2013**, *103*, 183113.
19. Walia, S.; Balendhran, S.; Wang, Y.; Ab Kadir, R.; Zoolfakar, A. S.; Atkin, P.; Ou, J. Z.; Sriram, S.; Kalantar-Zadeh, K.; Bhaskaran, M. Characterization of Metal Contacts for Two-Dimensional MoS_2 Nanoflakes. *Appl. Phys. Lett.* **2013**, *103*, 232105.
20. Du, Y.; Yang, L.; Liu, H.; Ye, P. D. Contact Research Strategy for Emerging Molybdenum Disulfide and Other Two-Dimensional Field-Effect Transistors. *APL Mater.* **2014**, *2*, 092510.
21. Sreeprasad, T. S.; Nguyen, P.; Kim, N.; Berry, V. Controlled, Defect-Guided, Metal-Nanoparticle Incorporation Onto MoS_2 *via* Chemical and Microwave Routes: Electrical, Thermal, and Structural Properties. *Nano Lett.* **2013**, *13*, 4434–4441.
22. Chuang, S.; Battaglia, C.; Azcatl, A.; McDonnell, S.; Kang, J. S.; Yin, X.; Tosun, M.; Kapadia, R.; Fang, H.; Wallace, R. M.; Javey, A. MoS_2 p-Type Transistors and Diodes Enabled by High Work Function MoO_x Contacts. *Nano Lett.* **2014**, *14*, 1337–1342.
23. McDonnell, S.; Azcatl, A.; Addou, R.; Gong, C.; Battaglia, C.; Chuang, S.; Cho, K.; Javey, A.; Wallace, R. M. Hole Contacts on Transition Metal Dichalcogenides: Interface Chemistry and Band Alignments. *ACS Nano* **2014**, *8*, 6265–6272.
24. McGovern, I. T.; Williams, R. H.; Mee, C. H. B. Electronic Properties of Cleaved Molybdenum Disulphide Surfaces. *Surf. Sci.* **1974**, *46*, 427.
25. McMenamin, J. C.; Spicer, W. E. Photoemission Studies of Layered Transition-Metal Dichalcogenides: MoS_2. *Phys. Rev. B* **1977**, *16*, 5474.
26. Kamaratos, M.; Papageorgopoulos, C. A. Adsorption Studies on Ar^+-Sputtered MoS_2(0001). *Surf. Sci.* **1986**, *178*, 865–871.
27. Schlaf, R.; Lang, O.; Pettenkofer, C.; Jaegermann, W. Band Lineup of Layered Semiconductor Heterointerfaces Prepared by Van der Waals Epitaxy: Charge Transfer Correction Term for the Electron Affinity Rule. *J. Appl. Phys.* **1999**, *85*, 2732.
28. Coy-Diaz, H.; Addou, R.; Batzill, M. Interface Properties of CVD Grown Graphene Transferred onto MoS_2 (0001). *Nanoscale* **2014**, *6* (628), 1071–1078.
29. Michaelson, H. B. The Work Function of the Elements and its Periodicity. *J. Appl. Phys.* **1977**, *48*, 4729.
30. Skriver, H. L.; Rosengaard, N. M. Surface Energy and Work Function of Elemental Metals. *Phys. Rev. B: Condens. Matter Mater. Phys.* **1992**, *46*, 7157.
31. Sachtler, W. M. H.; Dorgelo, G. J. H.; Holscher, A. A. The Work Function of Gold. *Surf. Sci.* **1966**, *5*, 221–229.
32. Kautek, W.; Gerischer, H.; Tributsch, H. The Role of Carrier Diffusion and Indirect Optical Transitions in the Photoelectrochemical Behavior of Layer Type d-Band Semiconductors. *J. Electrochem. Soc.* **1980**, *127*, 2471–2478.
33. Addou, R.; Colombo, L.; Wallace, R. M. Surface Defects on Natural MoS_2. *ACS Appl. Mater. Interfaces* **2015**, *7*, 11921–11929.
34. Kam, K. K.; Parkinson, B. A. Detailed Photocurrent Spectroscopy of the Semiconducting Group-VIB Transition-Metal Dichalcogenides. *J. Phys. Chem.* **1982**, *86*, 463.
35. Mak, K. F.; Lee, C.; Hone, J.; Shan, J.; Heinz, T. F. Atomically Thin MoS_2: A New Direct-Gap Semiconductor. *Phys. Rev. Lett.* **2010**, *105*, 136805.
36. Splendiani, A.; Sun, L.; Zhang, Y.; Li, T.; Kim, J.; Chim, C. Y.; Galli, G.; Wang, F. Emerging Photoluminescence in Monolayer MoS_2. *Nano Lett.* **2010**, *10*, 1271.
37. Wilson, J. A.; Yoffe, A. D. The Transition Metal Dichalcogenides Discussion and Interpretation of the Observed Optical, Electrical and Structural Properties. *Adv. Phys.* **1969**, *18*, 193.
38. Kuc, A. Low-Dimensional Transition-Metal Dichalcogenides. *Chem. Modell.* **2014**, *11*, 1–29.
39. Py, M. A.; Haering, R. R. Structural Destabilization Induced by Lithium Intercalation in MoS_2 and Related Compounds. *Can. J. Phys.* **1983**, *61*, 76–84.
40. Sandoval, S. J.; Yang, D.; Frindt, R. F.; Irwin, J. C. Raman Study and Lattice Dynamics of Single Molecular Layers of MoS_2. *Phys. Rev. B: Condens. Matter Mater. Phys.* **1991**, *44*, 3955.
41. Wypych, F.; Schöllhorn, R. 1T-MoS_2, a new Metallic Modification of Molybdenum Disulfide. *J. Chem. Soc., Chem. Commun.* **1992**, 1386–1388.
42. Papageorgopoulos, C. A.; Jaegermann, W. Li Intercalation Across and Along the Van der Waals Surfaces of MoS_2-(0001). *Surf. Sci.* **1995**, *338*, 83–93.
43. Wypych, F.; Weber, Th.; Prins, R. Scanning Tunneling Microscopic Investigation of 1T-MoS_2. *Chem. Mater.* **1998**, *10*, 723–727.
44. Eda, G.; Yamaguchi, H.; Voiry, D.; Fujita, T.; Chen, M.; Chhowalla, M. Photoluminescence from Chemically Exfoliated MoS_2. *Nano Lett.* **2011**, *11*, 5111–5116.

45. Kappera, R.; Voiry, D.; Yalcin, S. E.; Branch, B.; Gupta, G.; Mohite, A. D.; Chhowalla, M. Phase-Engineered Low-Resistance Contacts for Ultrathin MoS_2 Transistors. *Nat. Mater.* **2014**, *13*, 1128–1134.
46. Hagström, S.; Nordling, C.; Siegbahn, K. Electron Spectroscopic Determination of the Chemical Valence State. *Eur. Phys. J. A* **1964**, *178*, 439–444.
47. Dolui, K.; Rungger, I.; Das Pemmarajau, C.; Sanvito, S. Possible Doping Strategies for MoS_2 Monolayers: An *ab initio* Study. *Phys. Rev. B: Condens. Matter Mater. Phys.* **2013**, *88*, 075420.
48. Sarkar, D.; Xie, X.; Kang, J.; Zhang, H.; Liu, W.; Navarrete, J.; Moskovits, M.; Banerjee, K. Functionalization of Transition Metal Dichalcogenides with Metallic Nanoparticles: Implications for Doping and Gas-Sensing. *Nano Lett.* **2015**, *15*, 2852–2862.
49. Beauchemin, D. Inductively Coupled Plasma Mass Spectrometry. *Anal. Chem.* **2006**, *78*, 4111–4136.
50. Beebe, M.; Anderson, S. Monitoring Wafer Cleanliness and Metal Contamination *via* VPD ICP-MS: Case Studies for Next Generation Requirements. *Microelectron. Eng.* **2010**, *87*, 1701–1705.
51. *Defects in High-k Gate Dielectric Stacks*; Evgeni, G., Ed.; NATO Science Series II: Mathematics, Physics and Chemistry, Springer: 2006.
52. Sze, S. M.; Ng, K. K. *Physics of Semiconductor Devices*, 3rd ed.; Wiley: Hoboken, NJ, 2006.
53. Ma, N.; Jena, D. Charge Scattering and Mobility in Atomically Thin Semiconductors. *Phys. Rev. X* **2014**, *4*, 011043.
54. Ganta, D.; Sinha, S.; Haasch, R. T. 2-D Material Molybdenum Disulfide Analyzed by XPS. *Surf. Sci. Spectra* **2014**, *21*, 19.
55. Lince, J. R.; Fleischauer, P. D. Noble Gas Ion Bombardment of the Basal Plane Surface of MoS_2. *J. Vac. Sci. Technol., A* **1987**, *5*, 1312.
56. McIntyre, N. S.; Spevack, P. A.; Beamson, G.; Briggs, D. Effects of Argon Ion Bombardment on Basal Plane and Polycrystalline MoS_2. *Surf. Sci.* **1990**, *237*, L390–L397.
57. Hansen, W. N.; Hansen, G. J. Standard Reference Surfaces for Work Function Measurements in Air. *Surf. Sci.* **2001**, *481*, 172–184.
58. KC, S.; Longo, R. C.; Wallace, R. M.; Cho, K. Surface Oxidation Energetics and Kinetics on MoS_2 Monolayer. *J. Appl. Phys.* **2015**, *117*, 135301.
59. Pan, T.; Sun, L. Sub-Microscopic Phenomena of Metallic Corrosion Studied by a Combined Photoelectron Spectroscopy in Air (PESA) and Scanning Kelvin Probe Force Microscopy (SKPFM) Approach. *Int. J. Electrochem. Sci.* **2012**, *7*, 9325–9344.
60. KC, S.; Longo, R. C.; Addou, R.; Wallace, R. M.; Cho, K. Impact of Intrinsic Atomic Defects on the Electronic Structure of MoS_2 Monolayers. *Nanotechnology* **2014**, *25*, 375703.
61. Ichinokawa, T.; Ichinose, T.; Tohyama, M.; Itoh, H. Scanning Tunneling Microscopy Observation of MoS_2 Surface and Gold Clusters Deposited on MoS_2 Surface. *J. Vac. Sci. Technol., A* **1990**, *8*, 500.
62. Dahal, A.; Addou, R.; Coy-Diaz, H.; Batzill, M. Wet-Transfer of CVD-Grown Graphene onto Sulfur-Protected W(110). *Surf. Sci.* **2015**, *634*, 9–15.
63. Yue, R.; Barton, A. T.; Zhu, H.; Azcatl, A.; Pena, L. F.; Wang, J.; Peng, X.; Lu, N.; Cheng, L.; Addou, R.; et al. $HfSe_2$ Thin Films: 2D Transition Metal Dichalcogenides Grown by Molecular Beam Epitaxy. *ACS Nano* **2015**, *9*, 474–480.
64. Lin, Y.-C.; Chang, C.-Y. S.; Ghosh, R. K.; Liand, J.; Zhu, H.; Addou, R.; Diaconescu, B.; Ohta, T.; Peng, X.; Lu, N.; et al. Atomically Thin Heterostructures Based on Single-Layer Tungsten Diselenide and Graphene. *Nano Lett.* **2014**, *14*, 6936–6941.
65. Barton, A. T.; Yue, R.; Anwar, S.; Zhu, H.; Peng, X.; McDonnell, S.; Lu, N.; Addou, R.; Colombo, L.; Kim, M. J.; et al. Transition Metal Dichalcogenide and Hexagonal Boron Nitride Grown by Molecular Beam Epitaxy. *Microelectron. Eng.* **2015**, *147*, 306–309.
66. Frindt, R. F. Single Crystals of MoS_2 Several Molecular Layers Thick. *J. Appl. Phys.* **1966**, *37*, 1928.
67. MoS_2 crystals were purchased from two different suppliers: SPI vendor, http://www.2spi.com/ and 2D Semiconductors vendor, http://www.2dsemiconductors.com/.
68. Wallace, R. M. In-Situ Studies on 2D Materials. *ECS Trans.* **2014**, *64*, 109–116.
69. Powell, R. J. Interface Barrier Energy Determination from Voltage Dependence of Photoinjected Currents. *J. Appl. Phys.* **1970**, *41*, 2424.
70. Hashimoto, H.; Nakajima, K.; Suzuki, M.; Sasakawa, K.; Kimura, K. Improvement of Sensitivity in High-Resolution Rutherford Backscattering Spectroscopy. *Rev. Sci. Instrum.* **2011**, *82*, 063301.